



HHS Public Access

Author manuscript

Neuroimage. Author manuscript; available in PMC 2019 April 15.

Published in final edited form as:

Neuroimage. 2018 April 15; 170: 95–112. doi:10.1016/j.neuroimage.2016.07.007.

Functional atlas of the awake rat brain: a neuroimaging study of rat brain specialization and integration

Zhiwei Ma¹, Pablo Perez¹, Zilu Ma¹, Yikang Liu¹, Christina Hamilton², Zhifeng Liang¹, and Nanyin Zhang^{1,2,*}

¹Department of Biomedical Engineering, The Pennsylvania State University, University Park, 16802

²The Neuroscience Program, The Huck Institutes of Life Sciences, The Pennsylvania State University, University Park, PA, USA 16802

Abstract

Connectivity-based parcellation approaches present an innovative method to segregate the brain into functionally specialized regions. These approaches have significantly advanced our understanding of the human brain organization. However, parallel progress in animal research is sparse. Using resting-state fMRI data and a novel, data-driven parcellation method, we have obtained robust functional parcellations of the rat brain. These functional parcellations reveal the regional specialization of the rat brain, which exhibited high within-parcel homogeneity and high reproducibility across animals. Graph analysis of the whole-brain network constructed based on these functional parcels indicates that the rat brain has a topological organization similar to humans, characterized by both segregation and integration. Our study also provides compelling evidence that the cingulate cortex is a functional hub region conserved from rodents to humans. Together, this study has characterized the rat brain specialization and integration, and has significantly advanced our understanding of the rat brain organization. In addition, it is valuable for studies of comparative functional neuroanatomy in mammalian brains.

Keywords

resting-state functional connectivity; rat; whole-brain parcellation; specialization; integration

Introduction

Regional specialization and global integration are two major organizational principles of the brain. An optimal brain requires a suitable balance between local specialization and global

* **Address for correspondence:** Dr. Nanyin Zhang, Hartz Family Career Development Associate Professor, Department of Biomedical Engineering, The Huck Institutes of Life Sciences, The Pennsylvania State University, W-341 Millennium Science Complex, University Park, PA 16802, USA, nuz2@psu.edu.

Publisher's Disclaimer: This is a PDF file of an unedited manuscript that has been accepted for publication. As a service to our customers we are providing this early version of the manuscript. The manuscript will undergo copyediting, typesetting, and review of the resulting proof before it is published in its final citable form. Please note that during the production process errors may be discovered which could affect the content, and all legal disclaimers that apply to the journal pertain.

Conflict of interest: none.

integration of brain activity (Tononi et al., 1998). Traditionally, regional specialization is investigated by first spatially partitioning the whole brain into a number of distinct units using anatomical landmarks and/or cytoarchitectural features (Tzourio-Mazoyer et al., 2002). These units, or regions, are presumed to subserve specialized functions, and to be functionally homogeneous. Functional integration is then studied by elucidating the connectional architecture of the whole-brain network constructed using these brain units. While this approach is often successful, anatomy-based parcellation can be imprecise and insufficient to represent the true functional specialization of the brain as it does not consider the function of individual region, and it is not always the case that structure can predict function (Sporns, 2011).

An appealing alternative approach to study brain specialization and integration is to segregate functionally distinct brain regions according to their connectivity profiles (Cloutman and Lambon Ralph, 2012). This connectivity-derived parcellation is based on the premise that each functionally specialized brain region is characterized by a distinct connectivity profile. For instance, using resting-state functional magnetic resonance imaging (rsfMRI) technology (Biswal et al., 1995; Biswal et al., 2010; Fox and Raichle, 2007), researchers have obtained fine-grained functional parcellations of various brain structures such as the thalamus (Fan et al., 2015; Ji et al., 2016), striatum (Choi et al., 2012; Jung et al., 2014), numerous cortical regions (Cauda et al., 2010; Goulas et al., 2012; Kahnt et al., 2012; Kim et al., 2010; Long et al., 2014; Nelson et al., 2010; Zhang and Li, 2012), and even parcellations of the whole brain (Blumensath et al., 2013; Craddock et al., 2012; Gordon et al., 2016; Shen et al., 2013; Wig et al., 2014; Yeo et al., 2011). Without the presence of overt tasks, rsfMRI measures resting-state functional connectivity (RSFC) between different brain regions based on temporal correlations of spontaneously fluctuating blood oxygenation level-dependent (BOLD) signals (Biswal et al., 2010; Fox and Raichle, 2007). Thus, rsfMRI-based parcellation approaches aim to partition the brain by identifying similarities and differences in RSFC profiles, often without any anatomical constraints. Therefore, brain parcels obtained using these methods can be taken as functional atlases of the brain (Liang et al., 2011).

The identification of brain parcels based on their RSFC fingerprint has significantly enhanced our understanding of the spatial specialization of the human brain. Indeed, connectivity-based parcellation has not only replicated regions identified by histology-based techniques (Bzdok et al., 2013), but has also discovered functionally specialized subregions that cannot be differentiated using cytoarchitectonic methods (Clos et al., 2013). In addition, quantifying RSFC between brain parcels enables the construction of whole-brain networks, and thus, helps reveal the functional integration of the human brain.

In contrast to the great success of rsfMRI studies in humans, we have little knowledge of RSFC-based brain parcellations in animals (Becerra et al., 2011; Gozzi and Schwarz, 2016; Liang et al., 2011, 2014; Lu et al., 2012; Schroeder et al., 2016; Zhang et al., 2010). This is partially because animal rsfMRI experiments usually rely on anesthesia to immobilize animals, while anesthesia is a significant confound in connectivity-based parcellation given its profound impact on RSFC. Lack of such knowledge highlights a fundamental poverty of insight into the regional specialization and global integration of the animal brain. In

addition, considering the potential value in studying comparative functional neuroanatomy and translational models of brain disorders, robust whole-brain RSFC-based parcellations in animals are of critical need.

To bridge this gap, we have acquired and analyzed rsfMRI data in rats. To avoid any confounding effects of anesthesia on RSFC, all animals were scanned at the awake state using the awake animal imaging paradigm established in our lab (Liang et al., 2011, 2012a, b, 2014; Liang et al., 2013; Liang et al., 2015a; Liang et al., 2015b; Zhang et al., 2010). Using a novel, data-driven parcellation method, we have created robust functional parcellations of the rat brain with homogeneous within-parcel RSFC profiles. Using functional parcels obtained, the rat whole-brain network was constructed, and topological characteristics of this network were evaluated using graph theory analysis.

Materials and Methods

Animals

31 adult male Long–Evans rats (300–500 g) were used in the present study (the discovery sample). Data from 11 additional rats (the replication sample) used in previous publications (Liang et al., 2011, 2012b; Liang et al., 2013) were reanalyzed for the purpose of the present study. Animals were housed in Plexiglas cages and maintained on a 12 h light:12 h dark schedule at a temperature between 22 and 24 °C. They were provided with food and water *ad libitum*. All experiments were approved by the Pennsylvania State University Institutional Animal Care and Use Committee (IACUC).

MRI experiments

Rats were first acclimated to the MRI scanner environment and noise for seven days to minimize imaging-related motion and physiological changes. Detailed acclimation procedures were described in our previous publications (Liang et al., 2011, 2012a, b, 2014; Liang et al., 2013; Liang et al., 2015a; Liang et al., 2015b; Zhang et al., 2010). Before imaging, rats were briefly anesthetized using 2% isoflurane, then secured into a head restrainer with a built-in coil, and placed in a body tube. Isoflurane was discontinued after the setup was completed. rsfMRI data acquisition started at least 30 mins after the discontinuation of isoflurane. All rats were fully awake during all rsfMRI imaging sessions.

The MRI image acquisition of the discovery sample was conducted on a 7T magnet interfaced with a Bruker console. Anatomical images were acquired using a T1-weighted rapid imaging with refocused echoes (RARE) sequence with the following parameters: repetition time (TR) = 1500 ms; echo time (TE) = 8 ms; matrix size = 256 × 256; field of view (FOV) = 3.2 × 3.2 cm; slice number = 20; slice thickness = 1 mm; RARE factor = 8. T2*-weighted gradient-echo images covering the whole brain including the cerebrum were acquired using the echo planar imaging (EPI) sequence with the following parameters: TR = 1000 ms; TE = 15 ms; matrix size = 64 × 64; FOV = 3.2 × 3.2 cm; slice number = 20; flip angle = 60° and slice thickness = 1 mm. 600 volumes were acquired for each rsfMRI run, and two to four runs were obtained for each session.

The MRI image acquisition of the replication sample was conducted on a Bruker 4.7 T magnet. Anatomical images were acquired using a T1-weighted RARE sequence with the following parameters: TR = 2125 ms; TE = 50 ms; matrix size = 256×256 ; FOV = 3.2×3.2 cm; slice number = 18; slice thickness = 1 mm; and RARE factor = 8. T2*-weighted gradient-echo images were acquired using EPI sequence with the following parameters: TR = 1000 ms; TE = 30 ms; matrix size = 64×64 ; FOV = 3.2×3.2 cm; slice number = 18; and slice thickness = 1 mm. 600 volumes were acquired for each rsfMRI run, and six runs were obtained for each session.

Image preprocessing

Animals' motion was first estimated using the frame-wise displacement (FD) of each EPI volume according to the method described in (Power et al., 2012) with the parameters adjusted for the rat brain size. Specifically, FD was calculated using the parameters of geometric transformations (translation: $[x_i y_i z_i]$; rotation: $[\alpha_i \beta_i \gamma_i]$) obtained by the image intensity-based geometric transformation function in MATLAB ('imregtform') as follows (Power et al., 2012):

$$FD_i = |\Delta x_i| + |\Delta y_i| + |\Delta z_i| + |\Delta l_{\alpha_i}| + |\Delta l_{\beta_i}| + |\Delta l_{\gamma_i}|$$

where $x_i = |x_{i-1} - x_i|$ and $l_{\alpha_i} = |(\alpha_{i-1} - \alpha_i) \cdot r|$. Here, $r = 5$ mm, which is the approximate mean distance from the cortex to the center of the rat head. Volumes with $FD > 0.2$ mm and their immediate neighboring volumes were discarded. The first 10 volumes of each rsfMRI run were also discarded to ensure the magnetization to reach steady state. Runs with more than 10% of the total number of volumes discarded were excluded from further analysis.

Each animal was aligned and co-registered, based on anatomical images, to a fully segmented rat brain atlas embedded in Medical Image Visualization and Analysis software (MIVA <http://ccni.wpi.edu>). Motion correction was then performed using SPM12 (<http://www.fil.ion.ucl.ac.uk/spm/>), which corrects head motion using a rigid-body transformation model with three translational and three rotational parameters. These functional images were then spatially smoothed using a Gaussian kernel with an in-plane full-width-half-maximum (FWHM) of 0.75 mm. Six motion parameters estimated by SPM and signals from the white matter and ventricles were regressed out from the time series of each brain voxel. Band-pass filtering (0.01–0.1 Hz) was subsequently performed. To ensure the same degree of freedom for the calculation of RSFC (i.e. temporal Pearson correlation coefficient), 540 volumes were retained for each run after preprocessing.

Whole-brain RSFC-based parcellation

The RSFC profile of each individual gray matter voxel was obtained by seed-based correlational analysis. Specifically, the Pearson cross-correlation coefficients between the time course of the seed voxel and the time courses of all other gray matter voxels were respectively calculated. Correlation coefficients were transformed to Z values using Fisher's Z transformation. For each voxel, a group-level Z value map (i.e. RSFC profile) was obtained by one-sample t-test using a linear mixed-effect model with the random effect of rats and the fixed effect of z values. Subsequently, all RSFC profiles were clustered using the

k-means clustering approach, with the spatial dissimilarity between RSFC profiles as the distance. Consequently, this analysis generated a parcellation of the brain such that voxels with similar RSFC profiles are clustered together. The silhouette value was used to calculate the confidence value for each voxel within a parcel. Here, the silhouette value of a voxel measures how similar the RSFC profile of that voxel is to RSFC profiles of all other voxels in its own parcel, relative to voxels in different parcels. The clustering number (k) was within the range from 2 to 200. Results corresponding to two k values ($k = 40$ as an example of low-dimensionality clustering and $k = 130$ as an example of high-dimensionality clustering) were reported herein.

Parcel homogeneity

The homogeneity of individual parcels was evaluated using a method introduced in (Gordon et al., 2016). For each parcel, principal component analysis (PCA) was performed on normalized RSFC profiles (i.e. zero means and unit variance) of all voxels in the parcel, and parcel homogeneity (i.e. the homogeneity value) was computed as the percentage of the total variance explained by the first principal component (Gordon et al., 2016). The homogeneity of individual functional parcels was compared to that of a previously published anatomical atlas of the rat brain (Schwarz et al., 2006) derived from (Paxinos and Watson, 1998). The composite structures version of this atlas contained 48 parcels, in which two white matter parcels and a diminished gray matter parcel (raphe) due to downsampling to the EPI resolution were excluded from the analysis. The homogeneity value of each of the remaining 45 gray matter parcels of this anatomical parcellation was computed. For the comparison purpose, the same number functional parcels (i.e. 45) with the same overall spatial coverage were obtained to avoid the effect of parcel size on the homogeneity value, considering that the parcel homogeneity has been found to be related to parcel size (Gordon et al., 2016).

Reproducibility of functional parcels

Reproducibility of functional parcels was assessed by comparing the spatial maps of the corresponding parcels between two subgroups split from the discovery sample, or comparing the corresponding parcel maps between the discovery and replication samples. In the split-group approach, the discovery sample was randomly divided into two subgroups (16 rats in subgroup 1 and 15 rats in subgroup 2), and whole-brain RSFC-based parcellation was performed for each subgroup. Given a brain parcel from subgroup 1, the matched brain parcel from subgroup 2 was identified with the maximal Dice's coefficient (DC). DC for measuring the similarity between two brain parcels is defined as

$$DC = \frac{2|S_1 \cap S_2|}{|S_1| + |S_2|}$$

where $|S_1 \cap S_2|$ is the number of overlapped voxels of parcels 1 and 2, and $|S_1|$ is the number of voxels in parcel 1 and $|S_2|$ is the number of voxels in parcel 2. For the comparison between discovery and replication samples, the same matching method was applied.

Construction of the whole-brain functional network in the awake rat

The rat whole-brain network was constructed based on the parcellation with 130 parcels obtained from the discovery sample. Regionally averaged time course of each brain parcel was generated by averaging the time courses of all voxels within that brain parcel. RSFC was quantified by Pearson cross-correlation coefficient between the time courses of each pair of parcels, which was then converted to Z scores using Fisher's Z transformation. A group-level 130×130 RSFC matrix was generated by one-sample t-test using linear mixed-effect analysis with the random effect of rats and the fixed effect of z values. The whole-brain network was constructed with individual parcels as nodes and significant RSFC between parcels as edges.

Graph analysis of the rat brain network

Global graph metrics including average clustering coefficient, modularity, characteristic path length, global efficiency, small-worldness, and assortativity coefficient were quantified as a function of density in the range between 0.12 and 0.99 with a step size of 0.01. For each connection density, the graph was first binarized. Average clustering coefficient, characteristic path length and global efficiency were normalized to a reference network generated by randomizing the connectivity between parcels of the constructed network while maintaining the density. The randomization process was repeated 1000 times.

Local topological metrics of each brain parcel including node degree, local clustering coefficient, node characteristic path length and betweenness centrality were calculated based on the network binarized by setting a statistical threshold at $p < 0.05$ after FDR correction (Genovese et al., 2002). All these graph metrics were obtained using the Brain Connectivity Toolbox (<https://sites.google.com/site/bctnet/>), and their definitions can be found in (Rubinov and Sporns, 2010).

The identification of brain hubs in the rat brain network was performed on the same binarized network using the scoring method for “hubness” introduced in (van den Heuvel et al., 2010). A hub score between 0 and 4 was assigned to each node based on the number of the following criteria that the node satisfied: (1) top 20% highest degree; (2) top 20% highest betweenness centrality; (3) lowest 20% characteristic path length; (4) lowest 20% local clustering coefficient. Brain regions satisfied at least three out of these four criteria were identified as hubs.

To quantify the rich-club phenomenon in the rat brain network, the binarized network was pruned to construct subgraphs from 1 to the maximum degree, in a way that only the nodes with a degree greater than k ($N_{>k}$ nodes) were included in that specific level of subgraphs, and the rich-club coefficient $\phi(k)$ is defined as the ratio of remaining edges $E_{>k}$ in the k^{th} subgraph over the maximum possible number of edges ($N_{>k}(N_{>k} - 1)/2$) in that subgraph (Colizza et al., 2006):

$$\phi(k) = \frac{2E_{>k}}{N_{>k}(N_{>k} - 1)}$$

$\emptyset(k)$ was normalized to the mean of rich-club coefficient from 1000 reference networks, each of which was generated by randomizing the constructed network while maintaining the density (van den Heuvel and Sporns, 2011):

$$\emptyset_{norm}(k) = \frac{\emptyset(k)}{\emptyset_{random}(k)}$$

where $\emptyset_{random}(k)$ is the mean of rich-club coefficients of reference networks. The rich-club organization is present in the network if $\emptyset_{norm}(k) > 1$ for a continuous range of k (van den Heuvel and Sporns, 2011). A degree k' was identified for $\emptyset_{norm}(k') = \max(\emptyset_{norm}(k))$, and the nodes with the degree k' were identified as rich-club nodes in the network (Grayson et al., 2014).

Results

rsfMRI data in 31 awake rats were acquired on a 7T scanner (i.e. the discovery dataset). The RSFC profile of each individual gray matter voxel was obtained using seed-based correlational analysis. RSFC profiles for all voxels were then clustered using k-means clustering, such that voxels with similar RSFC profiles are clustered together. As a result, the whole rat brain was partitioned into a specific number of parcels (i.e. the parcel number: k). Brain parcellations with $k = 40$ (an example of a low-dimensionality parcellation) and $k = 130$ (an example of a high-dimensionality parcellation) are reported herein. A schematic summary of the data analysis procedure is shown in Figure 1.

Specialization of functional parcels in the awake rat brain

The rat brain specialization was revealed by RSFC-based parcellations. The spatial maps of individual functional parcels of the awake rat brain are shown in Figure 2 (40 parcels) and Figure 3 (130 parcels). All parcels were numbered based on their centroid locations (increasing in the caudal-rostral direction). Figures S1 (40 parcels) and S2 (130 parcels) revealed the global parcellation pattern by showing all parcels together. The majority of parcels were bilateral (36 out of 40 in the 40-parcel scheme; and 78 out of 130 in the 130-parcel scheme). The numbers of left and right unilateral parcels were approximately the same (40-parcel scheme: 2 right parcels and 2 left parcels; 130-parcel scheme: 27 right parcels and 25 left parcels).

Our data demonstrate that the connectivity-based parcellation was in general consistent with the histology-based anatomical atlas (Swanson, 2004). Each parcel was specifically located in a well-defined anatomical region/system, reflecting a convergence between anatomical and functional parcellations at a large scale. Given the consistency of the functional parcellation and anatomically defined brain regions, we grouped all parcels according to the anatomical system they belong to, including the brainstem, midbrain, thalamus/hypothalamus, amygdala, striatum, hippocampus/retrohippocampus, as well as cortical regions including visual, auditory, olfactory, somatosensory, motor, cingulate and prefrontal cortices. Detailed anatomical coverage of each individual parcel for the 40-parcel functional

atlas is listed in Table 1. Detailed anatomical coverage of each individual parcel for the 130-parcel functional atlas is listed in Table 2.

Despite the anatomy-function convergence at a large scale, the RSFC-based parcellations provided a more fine-grained segregation for individual brain structures that cannot be readily differentiated from anatomical images. For instance, the striatum appears to be a uniform structure in anatomical images. However, this system was divided into two subdivisions (Parcels 29 and 33) in a low-dimensionality functional parcellation (the 40-parcel scheme), including a dorsal (Parcel 29) and a ventral (Parcel 33) component. This separation well agrees with distinct functional roles that ventral and dorsal striatum play (Ferre et al., 2010; Taylor et al., 2013; Yager et al., 2015). An even finer parcellation of the striatum was observed in the 130-parcel atlas, with Parcel 74 located at the bilateral ventrocaudal caudoputamen (CPu), Parcel 93 at the left dorsal CPu, Parcel 94 at the right dorsal CPu, Parcel 96 at the bilateral mediodorsal CPu, Parcel 98 at the bilateral medioventral CPu, nucleus accumbens and lateral septal nucleus, Parcel 106 at the bilateral dorso-rostral CPu and 112 at the bilateral ventrorostral CPu and nucleus accumbens.

We further compared the within-cluster homogeneity between the RSFC-based and anatomical parcellations. The anatomical parcellation was selected based on an established atlas with 45 regions previously reported in an independent study (Schwarz et al., 2006). A functional parcellation with the same parcel number (i.e. 45) and spatial coverage was generated. For each parcel, PCA was performed on normalized RSFC profiles of all voxels in the parcel, and the within-parcel homogeneity was computed as the percentage of total variance explained by the first principal component (i.e. homogeneity value) (Gordon et al., 2016). Figure 4 shows that in general, functional parcels displayed higher homogeneity values than anatomical parcels (Figs. 4A and 4B). In addition, the anatomical parcellation had a large variation in parcel sizes, and its large-size parcels such as the somatosensory, visual and motor cortices as well as CPu had low homogeneity values. In contrast, the functional parcellation had a relatively small variation in parcel sizes, with high homogeneity values even for large-size parcels. More importantly, for the most majority of parcel sizes, the homogeneity value of the functional parcellation was above that of the anatomical parcellation, reflected by their Lowess fit curves (Fig. 4C). Taken together, these data suggest that RSFC-based parcellations can reveal functionally more specialized clusters than anatomical parcellations, and these functional parcels provide insight into our understanding of the regional specificity of the awake rat brain.

Robustness of RSFC-based parcellations

Regardless of the parcellation number, the spatial patterns of functional parcellations were highly robust, reflected by high reproducibility between separate groups of rats scanned in the same scanner, and even between rats scanned in different scanners with different magnetic field strengths. To evaluate the reproducibility of individual parcels, we randomly split rsfMRI data from 31 rats into two subgroups ($n=16$ for subgroup 1 and $n = 15$ for subgroup 2). Figure 5 shows the spatial maps of individual parcels obtained from each subgroup (40 parcels). 34 out of all 40 parcels exhibited highly consistent spatial patterns between the two subgroups. Mean (\pm SD) DC of all matched parcel pairs was 0.56 (\pm 0.13).

Furthermore, we applied the same parcellation method to a dataset collected on a different scanner (4.7 T, the replication dataset). Remarkably, very similar parcel maps were also produced in 30 out of 40 parcels (Figure 6) (mean (\pm SD) DC = 0.49 (\pm 0.08)).

High reproducibility of the RSFC-based parcellation was found regardless of the parcel number chosen, as very similar results were obtained for a high-dimensionality parcellation (130 parcels, shown in Figure S3 for the split-group comparison and in Figure S4 for the cross-scanner comparison). For the split-group comparison, 120 out of 130 parcels displayed reproducible spatial patterns (mean (\pm SD) DC of all matched parcel pairs = 0.53 (\pm 0.15)). For the cross-scanner comparison, 99 parcels were reproducible (mean (\pm SD) DC of all matched parcel pairs = 0.47 (\pm 0.14)). Taken together, these results suggest that RSFC-based parcellations in the awake rat brain were highly robust.

Intrinsic organization of the awake rat brain network

After obtaining a robust whole-brain parcellation with high functional specialization, we further investigated the intrinsic organization of the brain network constructed with individual parcels as nodes and RSFC between parcels as edge. This network was assessed using graph theory analysis. Figure 7 shows the whole-brain network constructed based on the 130-parcel scheme. Separate anatomical systems are color coded including the brainstem, midbrain, thalamus/hypothalamus, amygdala, striatum, hippocampus/retrohippocampus and cortical regions including visual, auditory, olfactory, somatosensory, motor, cingulate and prefrontal cortices. Figure 8 summarizes several fundamental global topological measures of the rat brain network as a function of connection density. Specifically, topological matrices of average clustering coefficient and modularity were used to characterize brain network segregation; characteristic path length and global efficiency were used to characterize the network integration; small-worldness was used to assess the balance between the brain segregation and integration; and assortativity coefficient was used to analyze the network resilience.

The graph analysis indicates that the awake rat brain network organization demonstrated balanced regional segregation and global integration when the brain connectivity is relatively sparse. Specifically, when the connection density was smaller than 0.5, the brain network exhibited a level of clustering higher than random network (normalized clustering coefficient > 1). In addition, modularity, which gauges the degree to which the network can be divided into separate communities (Newman, 2004), also had a relatively high value. In terms of network integration measures, the rat brain network was characterized by a high level of information exchange efficiency, reflected by global efficiency similar to random networks (i.e. normalized global efficiency = ~ 1), and low characteristic path length (i.e. normalized characteristic path length = ~ 1) at virtually all densities. These results collectively imply a small-world organization of the rat brain network, characterized by balanced regional segregation and global integration. Indeed, after being normalized to random networks with the same density, the measure of small-worldness was larger than 1 at densities < 0.5 . Furthermore, the rat brain network had positive values of assortativity at low densities, which suggests that the network exhibited high resilience. However, when the brain connectivity is not sparse (connection density higher than 0.5), the brain network showed

diminished segregation (low modularity and normalized clustering coefficient = ~ 1), loss of small-world organization (small-worldness = ~ 1) and disassortative behavior (assortativity = ~ 0).

Brain integration in the awake rat was further investigated by examining hub regions in the rat brain network (Figure 9). The identification of brain hubs was performed using the scoring method for “hubness” introduced in (van den Heuvel and Sporns, 2011) based on four criteria: (1) top 20% highest degree; (2) top 20% highest betweenness centrality; (3) lowest 20% characteristic path length; (4) lowest 20% local clustering coefficient. Brain regions satisfy at least three out of these four criteria were identified as functional hubs. According to these criteria, we found a list of hub regions in the awake rat brain, including bilateral temporal association cortex, bilateral entorhinal and perirhinal cortices, lateral area of right secondary visual cortex, right primary somatosensory cortex, right auditory cortex, right secondary somatosensory cortex, bilateral insular cortex, bilateral cingulate cortex, bilateral piriform cortex, right dorsal CPu, thalamus, and lateral hypothalamus. Due to their relatively high connectivity, these hub regions are likely to play central roles in brain information integration.

Figure S5 shows the spatial distribution of rich club regions in the rat brain. The rich-club phenomenon of a network is characterized by a greater connectedness among the highest-degree nodes relative to with lower-degree nodes, and therefore, these highest-degree nodes form a thickly interconnected ‘club’ within the network (Colizza et al., 2006). Fig. S5a shows the measured (ϕ) and normalized (ϕ_{norm}) rich-club coefficient as a function of degree for the rat brain network. Normalized rich-club coefficient clearly shows the presence of rich-club organization in the awake rat brain, with $\phi_{norm}(k) > 1$ for a continuous range of node degree. Rich-club regions in the rat brain include the right temporal association cortex, right entorhinal and perirhinal cortices, lateral area of right secondary visual cortex, right dorsolateral entorhinal cortex, bilateral auditory cortex, bilateral insular cortex, bilateral cingulate cortex, bilateral piriform cortex, right dorsal CPu and thalamus (Fig. S5). Taken together, these results suggest the awake rat brain network was highly integrated with distributed hub and rich-club regions.

Discussion

In the present study, we investigated both the specialization and integration of the awake rat brain. The brain specialization was studied by parcellating the whole brain into a number of functionally homogeneous parcels, using the criterion that brain voxels' RSFC profiles were similar within each parcel but dissimilar between parcels (Figs. 2 and 3). We have shown that this connectivity-based parcellation was in general consistent with the anatomical parcellation at a large scale, albeit it provided more fine-grained specialization and better within-parcel homogeneity than anatomically defined regions. In addition, regardless of the parcel number and scanner, functional parcellations obtained were highly robust. The brain integration was further investigated by constructing a whole-brain functional network based on functional parcels. Using a graph-theory approach, the topological organization of the whole-brain network was elucidated, functional hubs were identified (Figure 9), and a rich-club organization was observed (Figure S5).

Robust functional atlas revealed by RSFC-based parcellation in the awake rat brain

Since Brodmann segregated the cortex into cytoarchitectonically defined regions, the specialization of brain regions has largely been inferred from anatomical definitions. Since such definitions rarely take the functional aspects of brain regions into account, they can obfuscate differences in specialization amongst subregions.

RSFC-based parcellation has emerged as a powerful tool to parcellate a region of interest (ROI) in the human brain into functionally more homogeneous subdivisions. This approach has been used to elucidate functional subdivisions of the thalamus (Fan et al., 2015; Zhang et al., 2008), striatum (Choi et al., 2012; Jung et al., 2014), Broca's area (Kelly et al., 2010), orbitofrontal cortex (Kahnt et al., 2012), lateral frontal cortex (Goulas et al., 2012), medial frontal cortex (Kim et al., 2010), lateral parietal cortex (Nelson et al., 2010), sensorimotor cortex (Long et al., 2014), precuneus (Zhang and Li, 2012), and posteromedial cortex (Cauda et al., 2010). Using similar methods, whole-brain parcellations have also been achieved in the human (Blumensath et al., 2013; Craddock et al., 2012; Gordon et al., 2016; Shen et al., 2013; Wig et al., 2014; Yeo et al., 2011). These studies have provided great value for understanding the specialization at both the local and global scales of the human brain (Eickhoff et al., 2015).

Nevertheless, connectivity-based parcellation in the rodent brain is sparse (Gozzi and Schwarz, 2016; Liang et al., 2011; Schroeder et al., 2016). A lack of reliable functional parcellations has significantly hindered the advancement of rsfMRI studies in animal models, since the selection of ROIs directly from a histology-based atlas may not be optimal for either seed-based or graph analyses of rsfMRI data (Smith et al., 2011; Wang et al., 2009). In the present study, by clustering voxelwise RSFC profiles, we obtained low- and high-dimensional functional atlases with similar RSFC profiles for the voxels within each parcel. This voxelwise parcellation approach is completely data driven, as it utilized the information of rsfMRI data without any prior assumptions of ROIs before parcellation. Notably, we also avoided the confounding effects of anesthesia by using awake rats in our rsfMRI data acquisition (Liang et al., 2012b).

We found that all functional parcels obtained were located in anatomically well-defined regions, suggesting that functional parcellations provided brain segregations in general consistent with anatomical definitions. However, functional parcellations can further differentiate separate subdivisions of anatomically homogeneous brain structures. For instance, even in a low-dimensionality parcellation (e.g. 40 parcels), the ventral and dorsal striatum were well separated, despite the uniform contrast of the structure in anatomical MRI images. Functionally, it is well known that ventral and dorsal striatum play distinct roles. The ventral striatum, in particular the nucleus accumbens, primarily mediates reward, reinforcement and motivational salience behaviors, whereas the dorsal striatum mainly mediates cognition involving motor and executive functions, as well as stimulus-response learning (Ferre et al., 2010; Taylor et al., 2013; Yager et al., 2015). Taken together, these results indicate that the RSFC-based parcellation approach is sensitive to functional specificity and offers a great tool to investigate the brain specialization in the animal.

Importantly, functional parcels of the rat brain obtained were highly robust, reflected by high reproducibility across data acquired in the same scanner, or even across different MRI scanners. This robustness is essential for establishing a standard functional atlas of the awake rodent brain. In addition, a robust parcellation is critically important for studying the brain network organization as unstable parcellations will have significant influences on measuring network topological properties (Wang et al., 2009). Furthermore, the same parcellation approach can be readily extended to analyzing rsfMRI data in other species.

Topological characteristics of the awake rat brain network

By constructing the whole-brain network of the awake rat based on functional parcels obtained, we further investigated the rat brain organization in terms of network segregation, global integration and resilience. Since all network topological matrices are sensitive to the network connection density, we assessed these topological measures in a large range of density.

Our data (Fig. 8) indicate that at relatively low densities (density < 0.5), the rat brain network exhibited high levels of segregation while maintained high efficiency in information integration (i.e. high integration), reflected by high clustering coefficient and modularity but comparable global efficiency and characteristic path length relative to random networks with the same densities. These characteristics together demonstrate small-worldness, a characterizing feature of human brain networks (Sporns and Honey, 2006). At similar densities, the network also displayed a positive assortativity, which suggests the presence of a resilient core of interconnected hubs that are against targeted attacks. By contrast, the rat brain network showed distinct characteristics that were indistinguishable from random networks at density > 0.5 . This observation was consistent with a recent study that reported a heavily connected network (density = 0.66) in the macaque brain, which does not show a small-world organization (Markov et al., 2013; Markov et al., 2014). In addition, at high densities the rat brain network had zero to negative assortativity, which suggests that a hub tends to be connected to non-hubs, and thus the network is vulnerable to targeted attacks (Rubinov and Sporns, 2010).

Global integration of the awake rat brain network

To further investigate functional integration of the awake rat brain network, we examined functional hubs and rich club regions of the network. Functional hubs are arguably the most important nodes in a brain network, considering the integrative role that hub nodes play. A functional hub is central in the network for efficient information transfer and integration in the brain (Bullmore and Sporns, 2009). In graph analysis, a hub node manifests the properties of high node degree, high betweenness centrality, short distance to other nodes in the network and low local clustering coefficient (Bullmore and Sporns, 2009). We identified a number of brain hubs including the ectorhinal, perirhinal, temporal association, cingulate, insular and piriform cortices (Figure 9), and these results are mostly in agreement with anatomical hubs previously identified in the rat brain (van den Heuvel et al., 2015), which suggests a convergence of brain hubs in anatomical and functional networks.

Functional integration can also be reflected by the rich-club organization of the network. It has been shown in humans that highest-degree node regions are also highly mutually interconnected, forming a 'rich club' of brain areas that are crucial for efficient brain communication (Colizza et al., 2006; van den Heuvel and Sporns, 2011). In the present study we identified a list of rich-club regions in the rat brain, including the right temporal association cortex, right entorhinal and perirhinal cortices, lateral area of right secondary visual cortex, right dorsolateral entorhinal cortex, bilateral auditory cortex, bilateral insular cortex, bilateral cingulate cortex, bilateral piriform cortex, right dorsal CPU, and thalamus. Taken together, these results suggest the rat brain network is highly integrated.

An interesting observation of the present study is that some brain hubs and rich-club regions were only present on the right side of the rat brain. Notably, only male rats were included in the present study and the right neocortex of male rats has been found to be thicker than the left neocortex (Diamond et al., 1975). These results suggest that the right neocortex of the male rat brain may play a more important role than the left in information processing.

Comparative functional neuroanatomy between humans and rodents

The successful translation of animal research relies on an effective understanding of how features have been conserved between humans and other species. In neuroscience, human functional connectivity studies have shown great promise in revealing organizational characteristics of brain networks in both healthy and pathological conditions. The potential of animal research to move these investigations forward remains largely untapped, in part because the conservation of the brain organization between species remains unclear. To address this problem, in the present study we have provided a robust functional atlas of the rat brain and analyze the similarity of its organization to the human brain.

Our data indicate that the rat brain network conserved fundamental topological properties as the human brain. Table 3 compared the topological matrices of the rat brain network measured in the present study with those of the human brain network reported in a study using a similar number of nodes (116 nodes in the human brain network and 130 nodes in the rat brain network) at three densities (0.15, 0.20, 0.25) (Sinclair et al., 2015). The comparison shows that all topological measures are quantitatively similar between the human and rat brain networks at all densities. Both species exhibit high levels of segregation and integration of their brain networks. This comparison indicates that the rat brain network shares significant topological features with the human brain, and highlights the translational value of the present study.

Another interesting question is that whether hub regions are conserved across humans and rodents. Previous human and mouse studies consistently singled out the cingulate cortex as a brain hub and/or a rich-club region in both structural and functional networks (Buckner et al., 2009; Grayson et al., 2014; Liska et al., 2015; van den Heuvel et al., 2010). Interestingly, we also found that the cingulate cortex was a brain hub in the awake rat brain as well. Furthermore, our data showed that rat functional network has a rich-club organization, which is a feature shared by human brain networks and the rat anatomical brain networks (Grayson et al., 2014; van den Heuvel et al., 2016; van den Heuvel and Sporns, 2011). Taken

together, these findings provide compelling evidence that the cingulate cortex is a functional hub region conserved across species.

Potential Limitations

There are a couple of technical limitations in the present study. First, the two parcellation numbers selected (40 and 130) are rather arbitrary. It should be noted that any parcellation scheme with a finite number of partitions is only an approximate representation of the functional organization of the brain (Moreno-Dominguez et al., 2014). In general, a low-dimensionality parcellation represents a 'coarse' partition of the brain, whereas a high-dimensionality parcellation represents a 'fine' partition of the brain. On the other hand, a low-dimensionality parcellation typically has a higher signal-to-noise ratio than a high-dimensionality parcellation. Precise determination of the optimal parcellation number remains a topic of active research in the field.

Another limitation is that the optimal method to threshold RSFC during brain graph construction is still somewhat controversial. The question is whether the threshold should be based on the statistical significance of RSFC, or based on the density (De Vico Fallani et al., 2014). Statistics-based thresholding methods have a straightforward statistical interpretation of the brain graph constructed, but are susceptible to non-neuronal physiological confounds. Meanwhile, sparsity-based thresholding methods can precisely control the density of the graph, but the graph construction can be more or less arbitrary. In the present study, to avoid the arbitrary nature of a single density, we reported global topological matrices within a reasonable range of densities that keep the whole-brain graph as one connected component. When a single threshold is necessary when computing nodal graph metrics, we applied the false-discovery rate (FDR) correction to determine the statistical significance of RSFC.

Only male rats were used in the present study. Since gender effects on RSFC have been identified in the human brain (Agcaoglu et al., 2015; Allen et al., 2011; Scheinost et al., 2015), it should be also interesting to include female rats in future studies and investigate the relationship between gender and RSFC in awake rats. Furthermore, the EPI spatial resolution applied in the present study is moderate. It is expected that a higher EPI spatial resolution should reduce the partial volume effect, which will in principle render a sharper transition between RSFC profiles across different brain regions, and thereby should further improve the parcellation quality.

Summary

The present study developed a functional atlas of the awake rat brain and studied the topographical features displayed by a whole-brain network based on that atlas. Highly reproducible functional parcels that were both (within-parcel) homogeneous and (between-parcel) specialized have been obtained. By constructing and analyzing the whole-brain network based on functional parcels, we found numerous hub regions in the awake rat brain that displayed structure-function convergence, and found a number of topological properties that preserved across mammalian brains. These results have significantly advanced our understanding of the rat brain specialization and integration. They also provide great value for studies of comparative functional neuroanatomy.

The significance of our findings can also be extended to studies of translational models for neuropsychiatric diseases. Accumulating evidence has shown that abnormalities of topological configurations of human brain networks are tightly linked to different brain disorders (Baggio et al., 2014; Buckner et al., 2009; Ray et al., 2014), suggesting that brain network topology may serve as a potential biomarker for various brain diseases. Thus, mapping the functional rat connectome at its normal state will provide an important reference point that will facilitate the identification of altered connectome topology in animal models of brain disease.

Supplementary Material

Refer to Web version on PubMed Central for supplementary material.

Acknowledgments

We would like to thank Ms. Lilit Antinori for editing the manuscript. The present study was supported by National Institute of Neurological Disorders and Stroke Grant R01NS085200 (PI: Nanyin Zhang, PhD) and National Institute of Mental Health Grant R01MH098003 (PI: Nanyin Zhang, PhD).

References

- Agcaoglu O, Miller R, Mayer AR, Hugdahl K, Calhoun VD. Lateralization of resting state networks and relationship to age and gender. *Neuroimage*. 2015; 104:310–325. [PubMed: 25241084]
- Allen EA, Erhardt EB, Damaraju E, Gruner W, Segall JM, Silva RF, Havlicek M, Rachakonda S, Fries J, Kalyanam R, Michael AM, Caprihan A, Turner JA, Eichele T, Adelsheim S, Bryan AD, Bustillo J, Clark VP, Feldstein Ewing SW, Filbey F, Ford CC, Hutchison K, Jung RE, Kiehl KA, Koditwakkum P, Komesu YM, Mayer AR, Pearlson GD, Phillips JP, Sadek JR, Stevens M, Teuscher U, Thoma RJ, Calhoun VD. A baseline for the multivariate comparison of resting-state networks. *Front Syst Neurosci*. 2011; 5:2. [PubMed: 21442040]
- Baggio HC, Sala-Llonch R, Segura B, Marti MJ, Valdeoriola F, Compta Y, Tolosa E, Junque C. Functional brain networks and cognitive deficits in Parkinson's disease. *Hum Brain Mapp*. 2014; 35:4620–4634. [PubMed: 24639411]
- Becerra L, Pendse G, Chang PC, Bishop J, Borsook D. Robust reproducible resting state networks in the awake rodent brain. *PLoS One*. 2011; 6:e25701. [PubMed: 22028788]
- Biswal B, Yetkin FZ, Haughton VM, Hyde JS. Functional connectivity in the motor cortex of resting human brain using echo-planar MRI. *Magn Reson Med*. 1995; 34:537–541. [PubMed: 8524021]
- Biswal BB, Mennes M, Zuo XN, Gohel S, Kelly C, Smith SM, Beckmann CF, Adelstein JS, Buckner RL, Colcombe S, Dogonowski AM, Ernst M, Fair D, Hampson M, Hoptman MJ, Hyde JS, Kiviniemi VJ, Kotter R, Li SJ, Lin CP, Lowe MJ, Mackay C, Madden DJ, Madsen KH, Margulies DS, Mayberg HS, McMahon K, Monk CS, Mostofsky SH, Nagel BJ, Pekar JJ, Peltier SJ, Petersen SE, Riedl V, Rombouts SA, Rypma B, Schlaggar BL, Schmidt S, Seidler RD, Siegle GJ, Sorg C, Teng GJ, Veijola J, Villringer A, Walter M, Wang L, Weng XC, Whitfield-Gabrieli S, Williamson P, Windischberger C, Zang YF, Zhang HY, Castellanos FX, Milham MP. Toward discovery science of human brain function. *Proc Natl Acad Sci U S A*. 2010; 107:4734–4739. [PubMed: 20176931]
- Blumensath T, Jbabdi S, Glasser MF, Van Essen DC, Ugurbil K, Behrens TE, Smith SM. Spatially constrained hierarchical parcellation of the brain with resting-state fMRI. *Neuroimage*. 2013; 76:313–324. [PubMed: 23523803]
- Buckner RL, Sepulcre J, Talukdar T, Krienen FM, Liu H, Hedden T, Andrews-Hanna JR, Sperling RA, Johnson KA. Cortical hubs revealed by intrinsic functional connectivity: mapping, assessment of stability, and relation to Alzheimer's disease. *J Neurosci*. 2009; 29:1860–1873. [PubMed: 19211893]
- Bullmore E, Sporns O. Complex brain networks: graph theoretical analysis of structural and functional systems. *Nat Rev Neurosci*. 2009; 10:186–198. [PubMed: 19190637]

- Bzdok D, Laird AR, Zilles K, Fox PT, Eickhoff SB. An investigation of the structural, connectional, and functional subspecialization in the human amygdala. *Hum Brain Mapp.* 2013; 34:3247–3266. [PubMed: 22806915]
- Cauda F, Geminiani G, D'Agata F, Sacco K, Duca S, Bagshaw AP, Cavanna AE. Functional connectivity of the posteromedial cortex. *PLoS One.* 2010; 5
- Choi EY, Yeo BT, Buckner RL. The organization of the human striatum estimated by intrinsic functional connectivity. *J Neurophysiol.* 2012; 108:2242–2263. [PubMed: 22832566]
- Clos M, Amunts K, Laird AR, Fox PT, Eickhoff SB. Tackling the multifunctional nature of Broca's region meta-analytically: co-activation-based parcellation of area 44. *Neuroimage.* 2013; 83:174–188. [PubMed: 23791915]
- Cloutman LL, Lambon Ralph MA. Connectivity-based structural and functional parcellation of the human cortex using diffusion imaging and tractography. *Front Neuroanat.* 2012; 6:34. [PubMed: 22952459]
- Colizza V, Flammini A, Serrano MA, Vespignani A. Detecting rich-club ordering in complex networks. *Nature Physics.* 2006; 2:110–115.
- Craddock RC, James GA, Holtzheimer PE 3rd, Hu XP, Mayberg HS. A whole brain fMRI atlas generated via spatially constrained spectral clustering. *Hum Brain Mapp.* 2012; 33:1914–1928. [PubMed: 21769991]
- De Vico Fallani F, Richiardi J, Chavez M, Achard S. Graph analysis of functional brain networks: practical issues in translational neuroscience. *Philos Trans R Soc Lond B Biol Sci.* 2014; 369
- Diamond MC, Johnson RE, Ingham CA. Morphological changes in the young, adult and aging rat cerebral cortex, hippocampus, and diencephalon. *Behav Biol.* 1975; 14:163–174. [PubMed: 1137540]
- Eickhoff SB, Thirion B, Varoquaux G, Bzdok D. Connectivity-based parcellation: Critique and implications. *Hum Brain Mapp.* 2015; 36:4771–4792. [PubMed: 26409749]
- Fan Y, Nickerson LD, Li H, Ma Y, Lyu B, Miao X, Zhuo Y, Ge J, Zou Q, Gao JH. Functional Connectivity-Based Parcellation of the Thalamus: An Unsupervised Clustering Method and Its Validity Investigation. *Brain Connect.* 2015; 5:620–630. [PubMed: 26106821]
- Ferre S, Lluís C, Justinova Z, Quiroz C, Orru M, Navarro G, Canela EI, Franco R, Goldberg SR. Adenosine-cannabinoid receptor interactions. Implications for striatal function. *Br J Pharmacol.* 2010; 160:443–453. [PubMed: 20590556]
- Fox MD, Raichle ME. Spontaneous fluctuations in brain activity observed with functional magnetic resonance imaging. *Nat Rev Neurosci.* 2007; 8:700–711. [PubMed: 17704812]
- Genovese CR, Lazar NA, Nichols T. Thresholding of statistical maps in functional neuroimaging using the false discovery rate. *Neuroimage.* 2002; 15:870–878. [PubMed: 11906227]
- Gordon EM, Laumann TO, Adeyemo B, Huckins JF, Kelley WM, Petersen SE. Generation and Evaluation of a Cortical Area Parcellation from Resting-State Correlations. *Cereb Cortex.* 2016; 26:288–303. [PubMed: 25316338]
- Goulas A, Uylings HB, Stiers P. Unravelling the intrinsic functional organization of the human lateral frontal cortex: a parcellation scheme based on resting state fMRI. *J Neurosci.* 2012; 32:10238–10252. [PubMed: 22836258]
- Gozzi A, Schwarz AJ. Large-scale functional connectivity networks in the rodent brain. *Neuroimage.* 2016; 127:496–509. [PubMed: 26706448]
- Grayson DS, Ray S, Carpenter S, Iyer S, Dias TG, Stevens C, Nigg JT, Fair DA. Structural and functional rich club organization of the brain in children and adults. *PLoS One.* 2014; 9:e88297. [PubMed: 24505468]
- Ji B, Li Z, Li K, Li L, Langley J, Shen H, Nie S, Zhang R, Hu X. Dynamic thalamus parcellation from resting-state fMRI data. *Hum Brain Mapp.* 2016; 37:954–967. [PubMed: 26706823]
- Jung WH, Jang JH, Park JW, Kim E, Goo EH, Im OS, Kwon JS. Unravelling the intrinsic functional organization of the human striatum: a parcellation and connectivity study based on resting-state FMRI. *PLoS One.* 2014; 9:e106768. [PubMed: 25203441]
- Kahnt T, Chang LJ, Park SQ, Heinzle J, Haynes JD. Connectivity-based parcellation of the human orbitofrontal cortex. *J Neurosci.* 2012; 32:6240–6250. [PubMed: 22553030]

- Kelly C, Uddin LQ, Shehzad Z, Margulies DS, Castellanos FX, Milham MP, Petrides M. Broca's region: linking human brain functional connectivity data and non-human primate tracing anatomy studies. *Eur J Neurosci*. 2010; 32:383–398. [PubMed: 20662902]
- Kim JH, Lee JM, Jo HJ, Kim SH, Lee JH, Kim ST, Seo SW, Cox RW, Na DL, Kim SI, Saad ZS. Defining functional SMA and pre-SMA subregions in human MFC using resting state fMRI: functional connectivity-based parcellation method. *Neuroimage*. 2010; 49:2375–2386. [PubMed: 19837176]
- Liang Z, King J, Zhang N. Uncovering intrinsic connectional architecture of functional networks in awake rat brain. *J Neurosci*. 2011; 31:3776–3783. [PubMed: 21389232]
- Liang Z, King J, Zhang N. Anticorrelated resting-state functional connectivity in awake rat brain. *Neuroimage*. 2012a; 59:1190–1199. [PubMed: 21864689]
- Liang Z, King J, Zhang N. Intrinsic organization of the anesthetized brain. *J Neurosci*. 2012b; 32:10183–10191. [PubMed: 22836253]
- Liang Z, King J, Zhang N. Neuroplasticity to a single-episode traumatic stress revealed by resting-state fMRI in awake rats. *Neuroimage*. 2014; 103:485–491. [PubMed: 25193500]
- Liang Z, Li T, King J, Zhang N. Mapping thalamocortical networks in rat brain using resting-state functional connectivity. *Neuroimage*. 2013; 83:237–244. [PubMed: 2377756]
- Liang Z, Liu X, Zhang N. Dynamic resting state functional connectivity in awake and anesthetized rodents. *Neuroimage*. 2015a; 104:89–99. [PubMed: 25315787]
- Liang Z, Watson GD, Alloway KD, Lee G, Neuberger T, Zhang N. Mapping the functional network of medial prefrontal cortex by combining optogenetics and fMRI in awake rats. *Neuroimage*. 2015b; 117:114–123. [PubMed: 26002727]
- Liska A, Galbusera A, Schwarz AJ, Gozzi A. Functional connectivity hubs of the mouse brain. *Neuroimage*. 2015; 115:281–291. [PubMed: 25913701]
- Long X, Goltz D, Margulies DS, Nierhaus T, Villringer A. Functional connectivity-based parcellation of the human sensorimotor cortex. *Eur J Neurosci*. 2014; 39:1332–1342. [PubMed: 24417550]
- Lu H, Zou Q, Gu H, Raichle ME, Stein EA, Yang Y. Rat brains also have a default mode network. *Proc Natl Acad Sci U S A*. 2012; 109:3979–3984. [PubMed: 22355129]
- Markov NT, Ercsey-Ravasz M, Van Essen DC, Knoblauch K, Toroczkai Z, Kennedy H. Cortical high-density counterstream architectures. *Science*. 2013; 342:1238406. [PubMed: 24179228]
- Markov NT, Ercsey-Ravasz MM, Ribeiro Gomes AR, Lamy C, Magrou L, Vezoli J, Misery P, Falchier A, Quilodran R, Gariel MA, Sallet J, Gamanut R, Huissoud C, Clavagnier S, Giroud P, Sappey-Marinié D, Barone P, Dehay C, Toroczkai Z, Knoblauch K, Van Essen DC, Kennedy H. A weighted and directed interareal connectivity matrix for macaque cerebral cortex. *Cereb Cortex*. 2014; 24:17–36. [PubMed: 23010748]
- Moreno-Dominguez D, Anwander A, Knosche TR. A hierarchical method for whole-brain connectivity-based parcellation. *Hum Brain Mapp*. 2014; 35:5000–5025. [PubMed: 24740833]
- Nelson SM, Cohen AL, Power JD, Wig GS, Miezin FM, Wheeler ME, Velanova K, Donaldson DI, Phillips JS, Schlaggar BL, Petersen SE. A parcellation scheme for human left lateral parietal cortex. *Neuron*. 2010; 67:156–170. [PubMed: 20624599]
- Newman ME. Fast algorithm for detecting community structure in networks. *Phys Rev E Stat Nonlin Soft Matter Phys*. 2004; 69:066133. [PubMed: 15244693]
- Paxinos, G. *The Rat Nervous System*. Elsevier Academic Press; Sydney, Australia: 2004.
- Paxinos, G., Watson, C. *The rat brain in stereotaxic coordinates*. 4th ed. Academic Press; San Diego: 1998.
- Power JD, Barnes KA, Snyder AZ, Schlaggar BL, Petersen SE. Spurious but systematic correlations in functional connectivity MRI networks arise from subject motion. *Neuroimage*. 2012; 59:2142–2154. [PubMed: 22019881]
- Ray S, Miller M, Karalunas S, Robertson C, Grayson DS, Cary RP, Hawkey E, Painter JG, Kriz D, Fombonne E, Nigg JT, Fair DA. Structural and functional connectivity of the human brain in autism spectrum disorders and attention-deficit/hyperactivity disorder: A rich club-organization study. *Hum Brain Mapp*. 2014; 35:6032–6048. [PubMed: 25116862]
- Rubinov M, Sporns O. Complex network measures of brain connectivity: uses and interpretations. *Neuroimage*. 2010; 52:1059–1069. [PubMed: 19819337]

- Scheinost D, Finn ES, Tokoglu F, Shen X, Papademetris X, Hampson M, Constable RT. Sex differences in normal age trajectories of functional brain networks. *Hum Brain Mapp.* 2015; 36:1524–1535. [PubMed: 25523617]
- Schroeder MP, Weiss C, Prociassi D, Disterhoft JF, Wang L. Intrinsic connectivity of neural networks in the awake rabbit. *Neuroimage.* 2016; 129:260–267. [PubMed: 26774609]
- Schwarz AJ, Danckaert A, Reese T, Gozzi A, Paxinos G, Watson C, Merlo-Pich EV, Bifone A. A stereotaxic MRI template set for the rat brain with tissue class distribution maps and co-registered anatomical atlas: application to pharmacological MRI. *Neuroimage.* 2006; 32:538–550. [PubMed: 16784876]
- Shen X, Tokoglu F, Papademetris X, Constable RT. Groupwise whole-brain parcellation from resting-state fMRI data for network node identification. *Neuroimage.* 2013; 82:403–415. [PubMed: 23747961]
- Sinclair B, Hansell NK, Blokland GA, Martin NG, Thompson PM, Breakspear M, de Zubicaray GI, Wright MJ, McMahon KL. Heritability of the network architecture of intrinsic brain functional connectivity. *Neuroimage.* 2015; 121:243–252. [PubMed: 26226088]
- Smith SM, Miller KL, Salimi-Khorshidi G, Webster M, Beckmann CF, Nichols TE, Ramsey JD, Woolrich MW. Network modelling methods for FMRI. *Neuroimage.* 2011; 54:875–891. [PubMed: 20817103]
- Sporns O. The human connectome: a complex network. *Ann N Y Acad Sci.* 2011; 1224:109–125. [PubMed: 21251014]
- Sporns O, Honey CJ. Small worlds inside big brains. *Proc Natl Acad Sci U S A.* 2006; 103:19219–19220. [PubMed: 17159140]
- Swanson, LW. *Brain Maps: Structure of the Rat Brain.* Elsevier; 2004.
- Taylor SB, Lewis CR, Olive MF. The neurocircuitry of illicit psychostimulant addiction: acute and chronic effects in humans. *Subst Abuse Rehabil.* 2013; 4:29–43. [PubMed: 24648786]
- Tononi G, Edelman GM, Sporns O. Complexity and coherency: integrating information in the brain. *Trends Cogn Sci.* 1998; 2:474–484. [PubMed: 21227298]
- Tzourio-Mazoyer N, Landeau B, Papathanassiou D, Crivello F, Etard O, Delcroix N, Mazoyer B, Joliot M. Automated anatomical labeling of activations in SPM using a macroscopic anatomical parcellation of the MNI MRI single-subject brain. *Neuroimage.* 2002; 15:273–289. [PubMed: 11771995]
- van den Heuvel MP, Mandl RC, Stam CJ, Kahn RS, Hulshoff Pol HE. Aberrant frontal and temporal complex network structure in schizophrenia: a graph theoretical analysis. *J Neurosci.* 2010; 30:15915–15926. [PubMed: 21106830]
- van den Heuvel MP, Scholtens LH, de Reus MA. Topological organization of connectivity strength in the rat connectome. *Brain Struct Funct.* 2015
- van den Heuvel MP, Scholtens LH, de Reus MA. Topological organization of connectivity strength in the rat connectome. *Brain Struct Funct.* 2016; 221:1719–1736. [PubMed: 25697666]
- van den Heuvel MP, Sporns O. Rich-club organization of the human connectome. *J Neurosci.* 2011; 31:15775–15786. [PubMed: 22049421]
- Wang J, Wang L, Zang Y, Yang H, Tang H, Gong Q, Chen Z, Zhu C, He Y. Parcellation-dependent small-world brain functional networks: a resting-state fMRI study. *Hum Brain Mapp.* 2009; 30:1511–1523. [PubMed: 18649353]
- Wig GS, Laumann TO, Petersen SE. An approach for parcellating human cortical areas using resting-state correlations. *Neuroimage.* 2014; 93(Pt 2):276–291. [PubMed: 23876247]
- Yager LM, Garcia AF, Wunsch AM, Ferguson SM. The ins and outs of the striatum: role in drug addiction. *Neuroscience.* 2015; 301:529–541. [PubMed: 26116518]
- Yeo BT, Krienen FM, Sepulcre J, Sabuncu MR, Lashkari D, Hollinshead M, Roffman JL, Smoller JW, Zollei L, Polimeni JR, Fischl B, Liu H, Buckner RL. The organization of the human cerebral cortex estimated by intrinsic functional connectivity. *J Neurophysiol.* 2011; 106:1125–1165. [PubMed: 21653723]
- Zhang D, Snyder AZ, Fox MD, Sansbury MW, Shimony JS, Raichle ME. Intrinsic functional relations between human cerebral cortex and thalamus. *J Neurophysiol.* 2008; 100:1740–1748. [PubMed: 18701759]

Zhang N, Rane P, Huang W, Liang Z, Kennedy D, Frazier JA, King J. Mapping resting-state brain networks in conscious animals. *J Neurosci Methods*. 2010; 189:186–196. [PubMed: 20382183]
Zhang S, Li CS. Functional connectivity mapping of the human precuneus by resting state fMRI. *Neuroimage*. 2012; 59:3548–3562. [PubMed: 22116037]

Author Manuscript

Author Manuscript

Author Manuscript

Author Manuscript

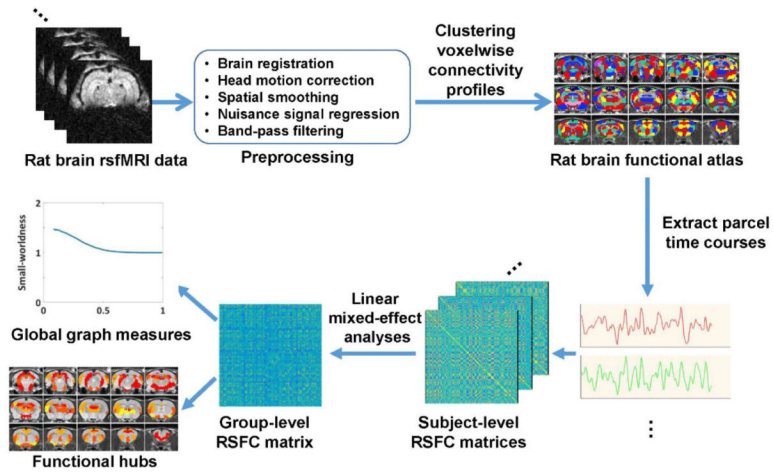


Figure 1.
Schematic illustration of the data analysis pipeline.

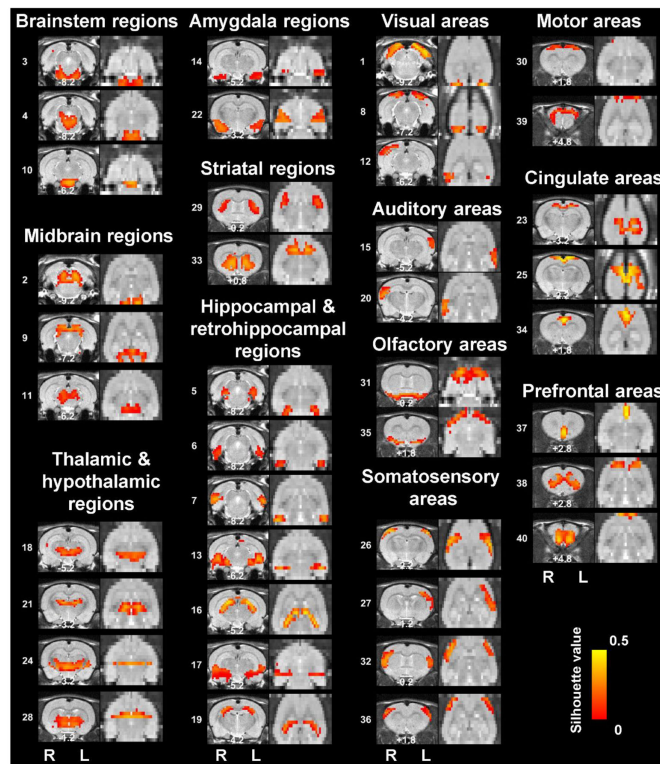


Figure 2. Low-dimensionality functional atlas obtained by the whole-brain RSFC-based parcellation (40 parcels)

Left columns are individual parcel maps overlaid on structural images (the coronal view) with the distance to the bregma (unit: mm) labeled at the bottom of each image. Right columns are individual parcel maps overlaid on structural images displayed in the axial view. Confidence (silhouette) values are used for color-coding voxels of brain parcels. Brain parcels are grouped based on the anatomical system they belong to, and they are numbered according to their centroid location in the caudal-rostral direction.

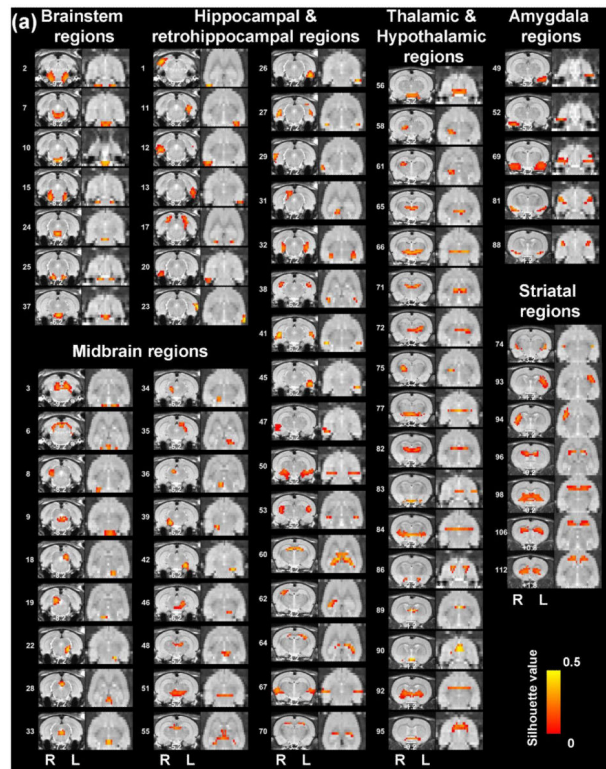


Figure 3. High-dimensionality functional atlas obtained by the whole-brain RSFC-based parcellation (130 parcels)

Left columns are individual parcel maps overlaid on structural images (the coronal view) with the distance to the bregma (unit: mm) labeled at the bottom of each image. Right columns are individual parcel maps overlaid on structural images displayed in the axial view. Confidence (silhouette) values are used for color-coding voxels of brain parcels. Brain parcels are grouped based on the anatomical system they belong to, and they are numbered according to their centroid location in the caudal-rostral direction.

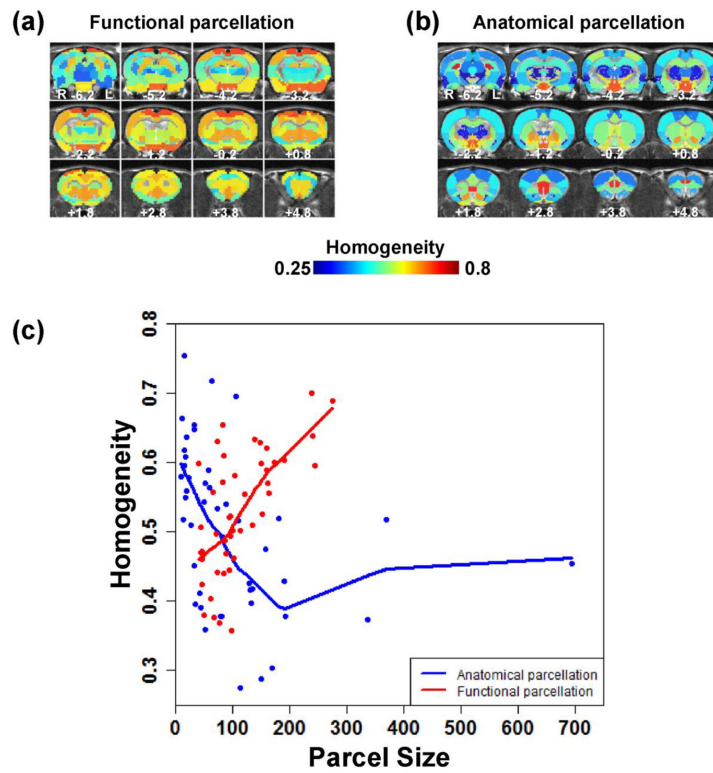
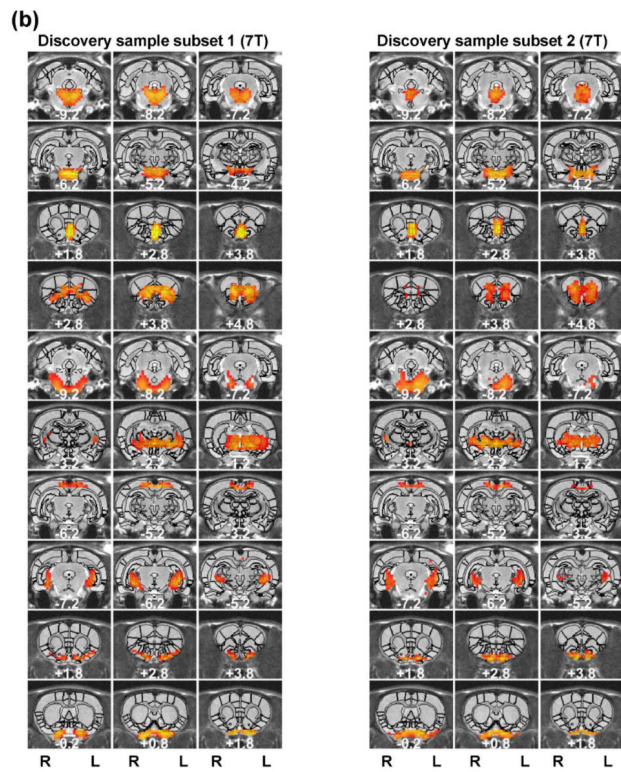
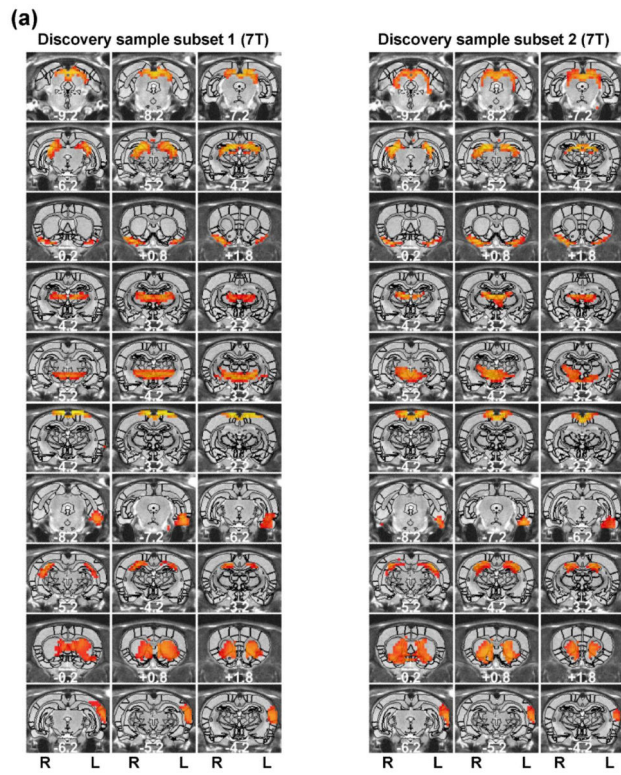


Figure 4. Comparison of parcel homogeneity between functional and anatomical parcellations (a) Parcel homogeneity map of the functional parcellation. (b) Parcel homogeneity map of the anatomical parcellation. (c) Homogeneity value plotted against parcel size for the two parcellation schemes. The homogeneity value of the functional parcellation is above that of the anatomical parcellation for the most majority of parcel sizes, reflected by their Lowess fit curves.



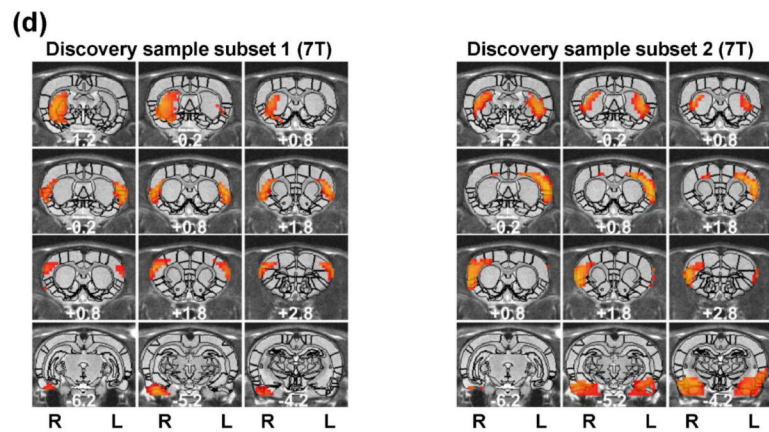
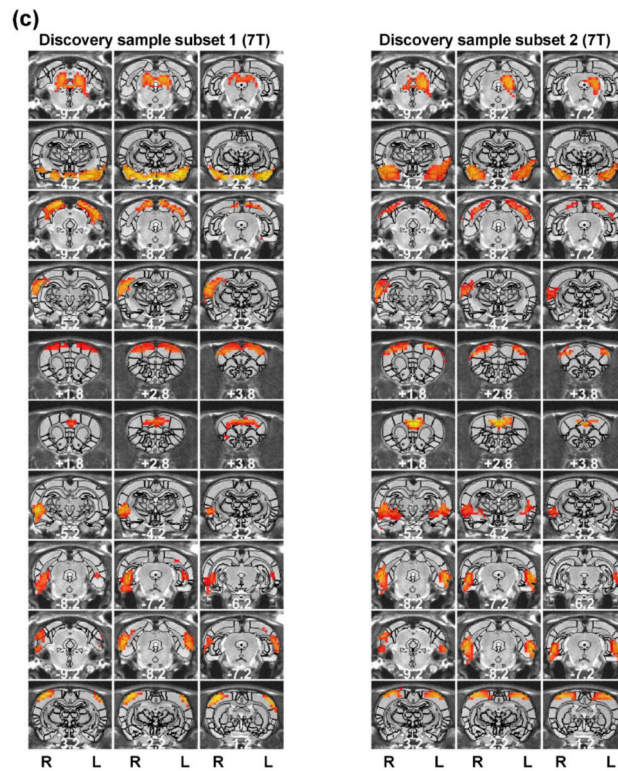
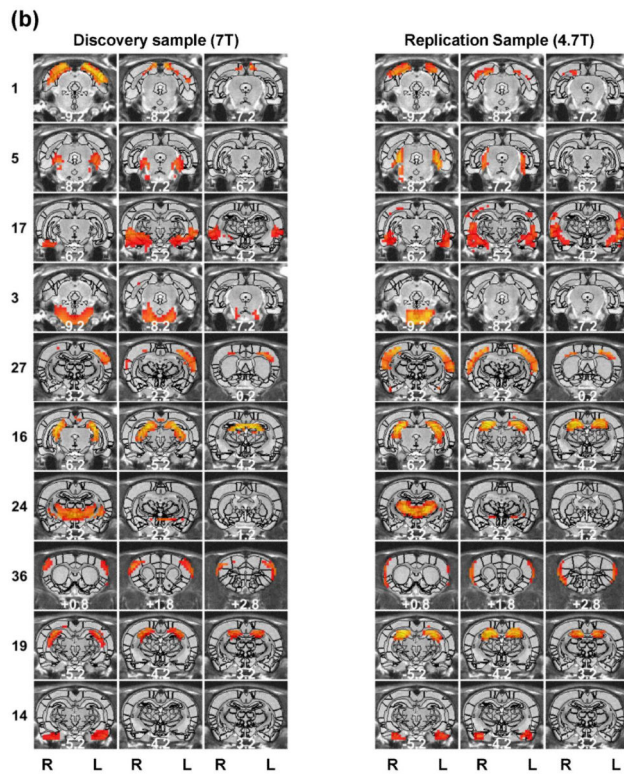
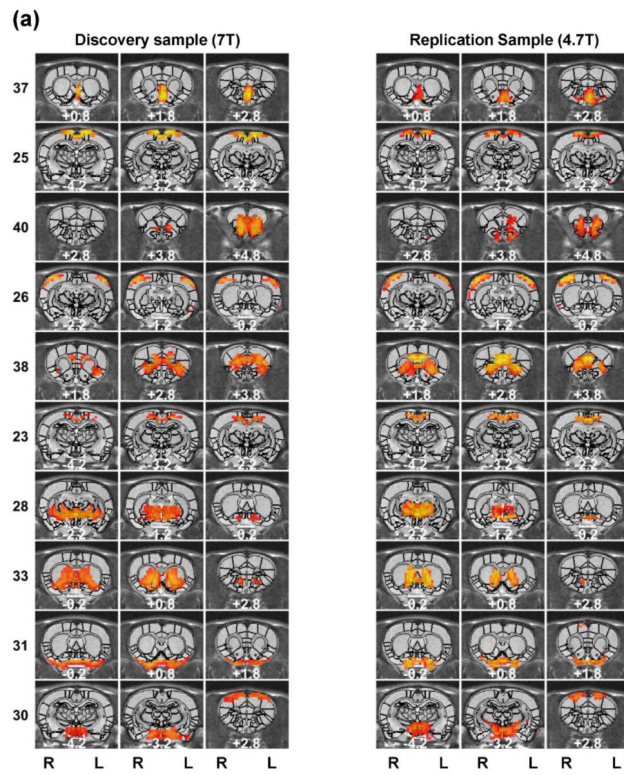


Figure 5. Reproducibility of the 40-parcel functional atlas evaluated using a split-group approach

Left (right) three columns are parcels obtained from the first (second) subset of the discovery sample. Brain parcels were matched between the two subsets based on the maximal DC. Distance to the bregma was labeled at the bottom of each image (unit: mm).



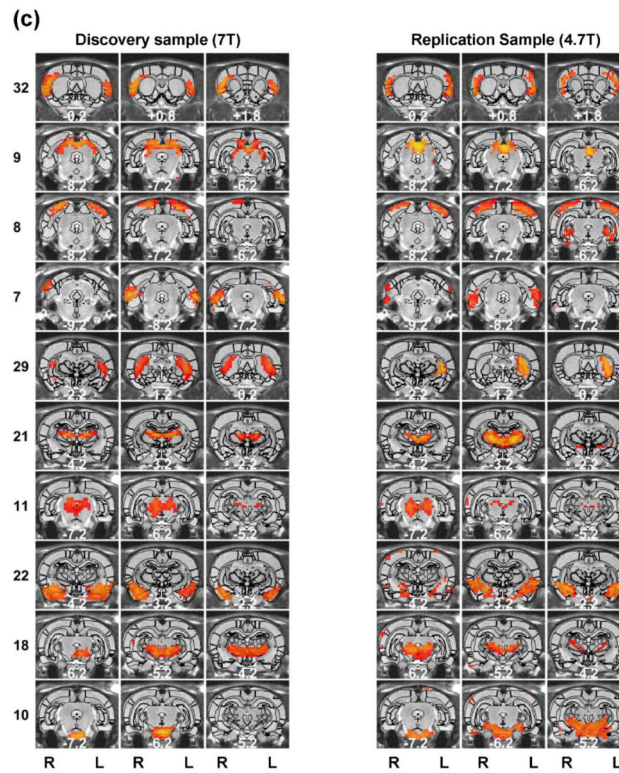


Figure 6. Reproducibility of the 40-parcel functional atlas between the discovery sample (7 T) and replication sample (4.7 T)

Left (right) three columns are parcels obtained from the discovery (replication) samples. Brain parcels were matched between the two samples according to the maximal DC. Distance to the bregma was labeled at the bottom of each image (unit: mm).

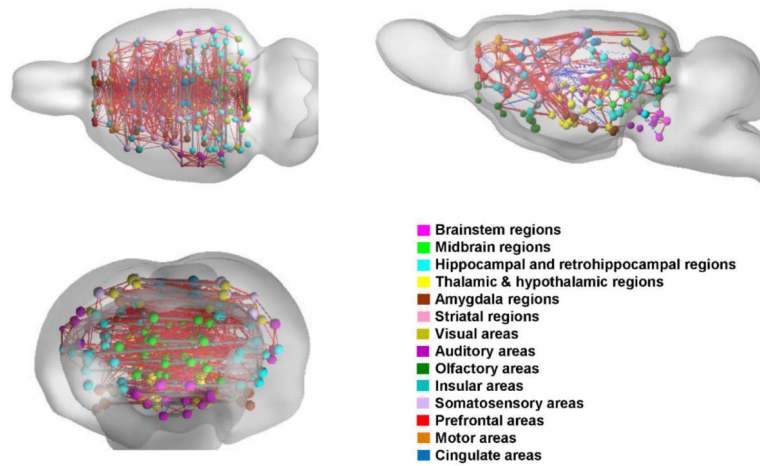


Figure 7. Rat whole-brain network constructed using 130 functional parcels

The network is visualized in the axial, sagittal and coronal views, respectively. Each ipsilateral parcel is represented by a node located at its centroid position with the node size proportional to the number of voxels of this parcel. For the display purpose only, each bilateral parcel is represented by two unilateral nodes, located at their corresponding ipsilateral centroid position and connected by a gray edge of uniform thickness. 8% of the strongest functional connections are displayed. Edges thickness is proportional to the RSFC strength. Red: positive connectivity; blue negative connectivity.

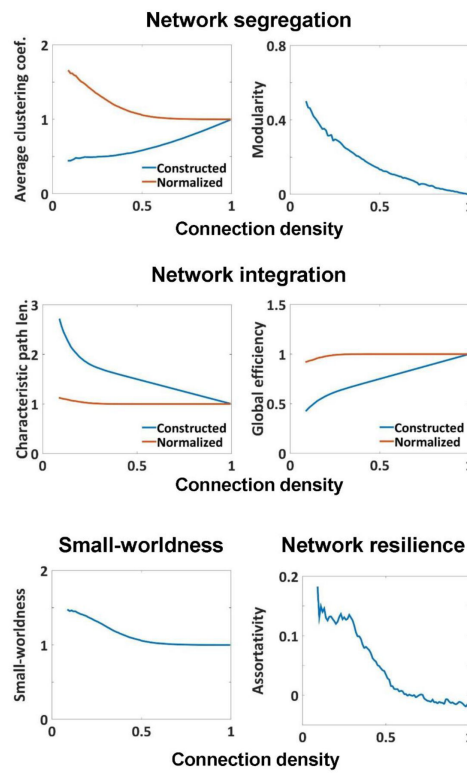


Figure 8. Global topological measures of the rat brain network

Network segregation is measured by average clustering coefficient and modularity. Network integration is measured by characteristic path length and global efficiency. Network segregation and integration balance is measured by small-worldness index. Network resilience is measured by assortativity coefficient.

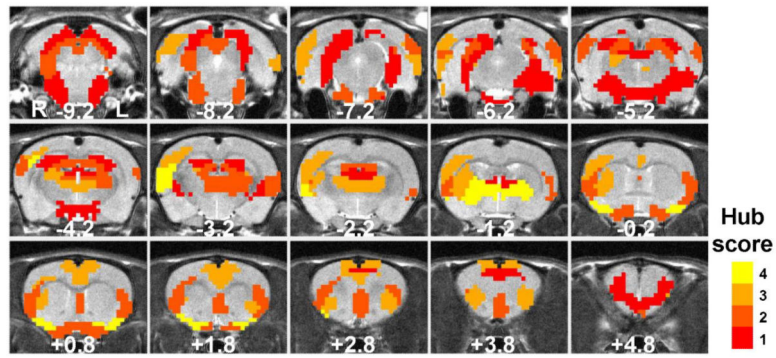


Figure 9. Hub regions of the rat brain network

Parcels with the hub score 1 are displayed. Parcels with a hub score 3 are identified as the functional hubs in the present study.

Table 1

Anatomical coverage of each parcel in the 40-parcel functional atlas of the awake rat brain.

System	Parcel #	Anatomical spatial coverage
brainstem regions	3	caudal part of pontine nuclei and subcoeruleus nucleus
	4	raphe nucleus, ventral periaqueductal gray, and isthmus reticular formation
	10	rostral part of pontine nuclei and reticular part of substantia nigra
midbrain regions	2	periaqueductal gray and central nucleus of inferior colliculus
	9	external cortex of inferior colliculus, dorsal cortex of inferior colliculus, retrosplenial cortex, dorsal superior colliculus, medial pretectal nucleus, and habenular nucleus
	11	periaqueductal gray, ventral superior colliculus, precuneiform nucleus, and reticular formation
thalamic and hypothalamic regions	18	mesencephalic reticular formation, zona incerta, and hypothalamus
	21	dorsal part of thalamus
	24	ventral part of thalamus
	28	ventral part of thalamus, globus pallidus and lateral hypothalamus
amygdala regions	14	caudal part of amygdala
	22	rostral part of amygdala
striatal regions	29	dorsal caudoputamen
	33	ventral caudoputamen and whole nucleus accumbens
hippocampal and retrohippocampal regions	5	caudomedial entorhinal cortex and parasubiculum
	6	dorsolateral and medial entorhinal cortex and transition area of subiculum
	7	caudal part of entorhinal cortex, perirhinal cortex, temporal association cortex, and transition area of subiculum
	13	ventral subiculum, ventrocaudal CA1 and ventrocaudal dentate gyrus
	16	postsubiculum, presubiculum, parasubiculum, dorsal CA1, rostral CA3 and dorsal dentate gyrus
	17	entorhinal cortex, perirhinal cortex, ventral CA1, and ventral CA3
visual areas	19	dorsal CA1
	1	retrosplenial cortex and caudal part of visual cortex
	8	rostral part of visual cortex
auditory areas	12	rostral part of visual cortex and parietal cortex
	15	left auditory cortex
somatosensory areas	20	right auditory cortex
	26	primary somatosensory cortex
	27	primary somatosensory cortex, and secondary somatosensory cortex
	32	primary somatosensory cortex, secondary somatosensory cortex, and posterior part of the insular cortex
olfactory areas	36	primary somatosensory cortex
	31	lateral hypothalamus, olfactory tubercle, and piriform cortex

System	Parcel #	Anatomical spatial coverage
	35	olfactory tubercle and piriform cortex, and a small portion of anterior part of the insular cortex
motor areas	30	primary motor cortex, secondary motor cortex, mammillary nucleus, and ventral hypothalamus
	39	primary motor cortex, secondary motor cortex, and a small portion of frontal cortex
cingulate areas	23	area 1 of cingulate cortex and ventral part of retrosplenial cortex
	25	ventral part of cingulate cortex, dorsal part of retrosplenial cortex, small portion of secondary visual cortex and secondary motor cortex
	34	area 2 of cingulate cortex
prefrontal areas	37	lateral septal nucleus, infralimbic cortex, dorsal peduncular cortex, and dorsal tenia tecta
	38	prelimbic cortex, orbital cortex, and insular cortex
	40	orbital cortex, anterior olfactory nucleus, prelimbic cortex, and piriform cortex

Author Manuscript

Author Manuscript

Author Manuscript

Author Manuscript

Table 2

Anatomical coverage of each parcel in the 130-parcel functional atlas of the awake rat brain.

System	Parcel #	Anatomical spatial coverage
brainstem regions	2	subcoeruleus nucleus
	7	pontine reticular nucleus
	10	pontine nuclei
	15	pontine nuclei, pontine reticular nucleus
	24	oral part of pontine reticular nucleus
	25	pontine nuclei
	37	pontine nuclei, interpeduncular nucleus
midbrain regions	3	lateral periaqueductal gray, central nucleus of inferior colliculus
	6	external cortex of inferior colliculus, dorsal cortex of inferior colliculus
	8	right external cortex of inferior colliculus
	9	raphe nucleus, tegmental nucleus, ventrolateral periaqueductal gray
	18	left central nucleus of inferior colliculus
	19	right central nucleus of inferior colliculus
	22	left precuneiform nucleus, isthmic reticular formation
	28	medial superior colliculus
	33	ventral periaqueductal gray
	34	right precuneiform nucleus, isthmic reticular formation, mesencephalic reticular formation
	35	left superficial gray layer of superior colliculus
	36	deep gray layer of superior colliculus
	39	right substantia nigra
	42	left substantia nigra
	46	mesencephalic reticular formation
48	deep gray layer of superior colliculus, pretectal nucleus	
51	parabrachial pigmented nucleus, red nucleus, reticular formation	
55	medial pretectal nucleus, habenular nucleus	
hippocampal and retrohippocampal regions	1	right entorhinal cortex, right perirhinal cortex
	11	left entorhinal cortex
	12	right entorhinal cortex, right perirhinal cortex, right perirhinal cortex
	13	left entorhinal cortex
	17	postsubiculum, parasubiculum, retrosplenial cortex
	20	right entorhinal cortex
	23	left entorhinal cortex, left perirhinal cortex, left temporal association cortex
	26	left entorhinal cortex
	27	presubiculum, transition area of subiculum
	29	right entorhinal cortex, right perirhinal cortex, right temporal association cortex
	31	right dorsal subiculum
	32	presubiculum, parasubiculum, dentate gyrus, CA3
38	dorsal CA1	

System	Parcel #	Anatomical spatial coverage
	41	CA1, CA3, dentate gyrus
	45	left CA1, left CA3, left dentate gyrus
	47	right entorhinal cortex, right ventral subiculum
	50	ventral CA1, ventral CA3, ventral dentate gyrus
	53	CA1, CA2, CA3
	60	dentate gyrus, CA1, CA3
	62	right CA1, right dentate gyrus
	64	left CA1, left dentate gyrus
	67	entorhinal cortex, perirhinal cortex
	70	CA1, CA2
	56	medial mammillary nucleus
	58	right anterior pretectal nucleus, right zona incerta, right ventral thalamic nucleus
	61	right lateral geniculate nucleus
	65	parafascicular thalamic nucleus, posterior thalamic nucleus group
	66	zona incerta, posterior hypothalamic nucleus
	71	dorsal thalamus
	72	left posterior thalamic nucleus group, ventral thalamic nucleus
	75	right posterior thalamic nucleus group, right ventral thalamic nucleus
thalamic and hypothalamic regions	77	lateral hypothalamus
	82	ventral thalamic nucleus
	83	lateral hypothalamus
	84	globus pallidus, zona incerta
	86	lateral hypothalamus
	89	stria medullaris of thalamus
	90	medial hypothalamus
	92	ventral thalamic nuclei
	95	lateral hypothalamus
	49	left amygdala
	52	right amygdala
amygdala regions	69	amygdala
	81	amygdala
	88	amygdala
	74	dorsocaudal caudoputamen
	93	left dorsal caudoputamen
	94	right dorsal caudoputamen
striatal regions	96	dorsal caudoputamen, lateral septal nucleus
	98	ventral caudoputamen, nucleus accumbens, lateral septal nucleus
	106	dorso-rostral caudoputamen
	112	ventro-rostral caudoputamen, nucleus accumbens
visual areas	4	monocular primary visual cortex, retrosplenial cortex

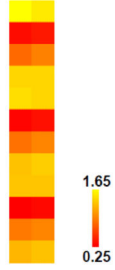
System	Parcel #	Anatomical spatial coverage
	5	binocular primary visual cortex, lateral area of secondary visual cortex
	14	lateral area of left secondary visual cortex, left temporal association cortex
	16	lateral area of right secondary visual cortex, right temporal association cortex
	21	primary visual cortex
	40	right primary visual cortex
	30	right auditory cortex, right temporal association cortex
	44	left auditory cortex, left temporal association cortex
auditory areas	54	right auditory cortex
	57	right auditory cortex
	59	left auditory cortex, left temporal association cortex
	76	right auditory cortex
	79	left auditory cortex
	100	olfactory tubercle
	104	piriform cortex
olfactory areas	109	olfactory tubercle, lateral septal nucleus
	115	olfactory tubercle, piriform cortex
	120	anterior olfactory nucleus
	128	anterior olfactory nucleus, piriform cortex
	130	anterior olfactory nucleus
	99	left insular cortex
	103	right insular cortex
insular areas	105	agranular insular cortex
	107	insular cortex, secondary somatosensory cortex
	116	left agranular insular cortex
	122	right agranular insular cortex
	63	left parietal cortex, left primary somatosensory cortex
	78	primary somatosensory cortex, secondary visual cortex
	80	primary somatosensory cortex
	85	primary somatosensory cortex, primary motor cortex
somatosensory areas	87	right primary somatosensory cortex, right secondary somatosensory cortex
	91	left primary somatosensory cortex, left secondary somatosensory cortex
	101	primary somatosensory cortex
	102	left primary somatosensory cortex, left secondary somatosensory cortex
	111	primary somatosensory cortex
	113	lateral septal nucleus, infralimbic cortex, dorsal peduncular cortex, dorsal tenia tecta
	119	prelimbic cortex
prefrontal areas	124	prelimbic cortex, orbital cortex
	125	secondary motor cortex
	129	dorsolateral orbital cortex

System	Parcel #	Anatomical spatial coverage
motor areas	114	right primary motor cortex, right secondary motor cortex
	117	primary motor cortex, secondary motor cortex
	118	primary motor cortex
	121	secondary motor cortex
	123	secondary motor cortex
	126	secondary motor cortex
	127	secondary motor cortex
cingulate areas	43	retrosplenial cortex
	68	retrosplenial cortex
	73	retrosplenial cortex, cingulate cortex
	97	cingulate cortex
	108	cingulate cortex
	110	cingulate cortex

Table 3

Comparisons of graph metrics between the human and rat brain.

Connection density	Graph metrics	Human brain (116 nodes, Sinclair et al., 2015)*	Rat brain (130 nodes, The present study)
0.15	average clustering coefficient	1.65	1.53
	modularity	0.32	0.40
	global efficiency	0.84	0.96
	small-worldness	1.41	1.43
0.20	average clustering coefficient	1.46	1.43
	modularity	0.28	0.34
	global efficiency	0.88	0.98
	small-worldness	1.31	1.38
0.25	average clustering coefficient	1.34	1.34
	modularity	0.25	0.30
	global efficiency	0.91	0.99
	small-worldness	1.24	1.32



* From Table S1a of Sinclair et al., 2015.

Author Manuscript

Author Manuscript

Author Manuscript

Author Manuscript